Science Advances

AAAS

Supplementary Materials for

Extending electron paramagnetic resonance to nanoliter volume protein single crystals using a self-resonant microhelix

Jason W. Sidabras*, Jifu Duan, Martin Winkler, Thomas Happe, Rana Hussein, Athina Zouni, Dieter Suter, Alexander Schnegg, Wolfgang Lubitz, Edward J. Reijerse*

*Corresponding author. Email: jason.sidabras@cec.mpg.de (J.W.S.); edward.reijerse@cec.mpg.de (E.J.R.)

This PDF file includes:

EPR characteristics comparison of multiple resonators. Comparison of resonator EPR characteristics were performed on an Elexsys E580 X-band bridge by Bruker Biospin. Four resonator geometries are used for this comparison. The Bruker Biospin i) dielectric ER4118X-MD-5W1 (MD5W1; sapphire ϵ_r of 11.5 parallel to C-axis and 9.3 perpendicular to C-axis) resonator and ii) Loop-gap resonator (LGR) ER4118X-MS-3W1 (MS3; split-ring) resonators are used as comparisons to known commercial resonator geometries. The dimensions of the MD5W1 and the MS3 can be found in Figs. S1A and S1B, respectively. Additionally, two Ω-shaped 0.5 mm ID planar micro-resonators (PMR) are also tested.(11-13) The first PMR uses iii) Rogers 6010LM (RO6010LM; Rogers Corp, Chandler, AZ, USA) substrate and one with (iv) sapphire substrate. The sapphire substrate was fabricated by Technical University Ilmenau (Ilmenau, Germany). Both PMR geometries have a 0.5 mm hole through the substrate which allows for a capillary sample to be placed in the center of the resonator. The general geometry for the PMR is shown in Fig. S1C.
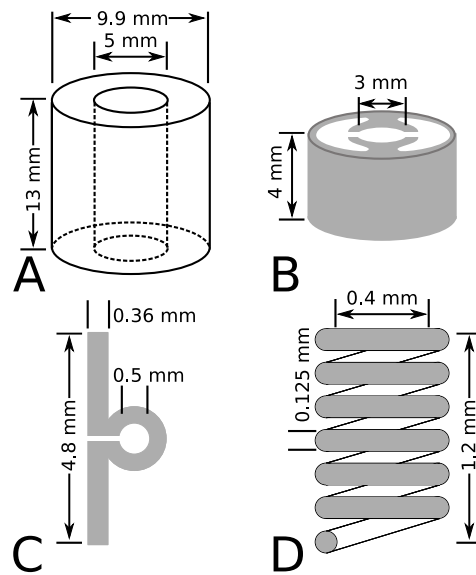
Fig. S1. Dimensions and geometry of the four resonators compared in this paper. A) Bruker Biospin ER4118X-MD-5W1 (MD5W1) sapphire dielectric resonator, B) Bruker Biospin ER4118X-MS-3W1 (MS3) split-ring resonator, C) Planar Micro Resonator 0.5 mm inner loop diameter, and D) selfresonant micro-helix with a 0.4 mm inner diameter. Gray indicates metallic surfaces.

Several other approaches have been followed to develop application-specific resonators for micro-samples: microstrip resonators (MR)(45-46), ultra-miniature micro-resonators (UMR, 2-150 μm) (47), surface loop-gap micro-resonators (LGMR, 50-150 μm) (48), very high-permittivity dielectric resonators (49,50), and planar micro-resonators (PMR).(11-13, 44) All of which significantly reduce the size of the resonator, but have challenges that limit the usefulness for single-crystal experiments.

The most promising of the previous work is the planar micro-resonator (PMR). The PMRs are fabricated by printing the micro-resonator geometry on a substrate using photo-lithographic techniques. (11-13) The planar micro-resonators show significant improvement in absolute spin sensitivity compared to the best commercial probe-heads available. (21) PMRs can be produced relatively cheaply using semiconductor etching techniques and laser scribing, and configured for many frequencies with inner diameter sample sizes of 20-1000 μm. Furthermore, these structures offer excellent filling factors, high resonator efficiencies, and minimal power dissipation. It was recently demonstrated that a planar micro-resonators with Rogers RO6010LM substrate and a 500 μm sample diameter can be successfully employed for the study of crystals of inorganic metal complexes as well as [NiFe]-hydrogenase ($0.35 \times 0.2 \times 0.2$ mm^3) at 14 GHz, equipped with a specially designed cryogenic receiver at a temperature of 12 K. (44) Yet, such designs require a modified bridge to accommodate the cryogenic amplifier setup.

Due to their planar geometry, PMR designs are limited in their Q-value (50-180) and suffer from a strong inhomogeneity of the microwave magnetic field, illustrated in Fig. S2A compared to the
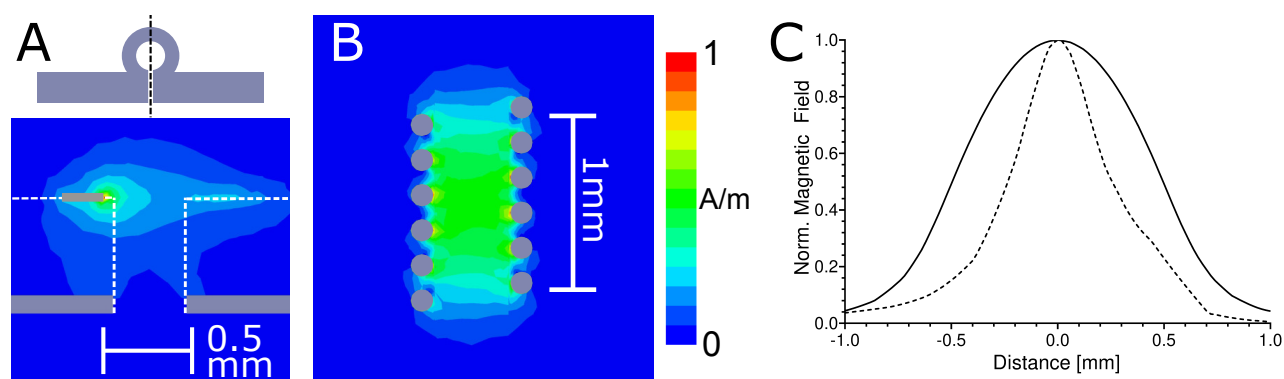
Fig. S2. Ansys HFSS finite-element modeling simulation of the microwave magnetic fields comparing the PMR and microhelix. Shown is the A) Ω-shaped planar micro-resonator on sapphire substrate (dashed white lines; cut-plane shown on inset) with a 0.5 mm sample diameter over a ground plane and a B) 5.5 turn micro-helix with a 0.4 mm inner diameter. Normalized microwave magnetic field, for both resonators at the same power, is shown on the right. C) Normalized microwave magnetic fields on axis of a Ω-shaped planar micro-resonators on sapphire substrate (dashed lines) with a 0.5 mm sample diameter over a ground plane and a 6.5 turn micro-helix with a 0.4 mm inner diameter (solid).

microwave magnetic field of the self-resonant micro-helix, Fig. S2B. The microwave magnetic field comparison on axis can be found in Fig. S2C. Improvement of the Q-value of the PMR geometry are reported here. By changing the substrate from Rogers RO6010LM substrate to single-crystal sapphire the Q-value increases by a factor of 3. The reduction of the Q-value using the Rogers RO6010LM substrate is partially due to surface roughness, and not just the loss tangent of the material. Because of these challenges, the PMRs have room for improvement and exploration of different geometries have led to the self-resonant micro-helix. Therefore, in this work, we compare the self-resonant micro-helix, general geometry shown in Fig. S1D, to the planar micro-resonators.

Simulations, from the commercially available finite-element modeling program Ansys Electronics Desktop with HFSS (High Frequency Structure Simulator; v. 19.1), network analyzer, and experimental measurements of resonator characteristics are tabulated in Table S1 and in Table 1 in the main text. Simulations are run assuming a 0.1 mm diameter by 0.1 mm height cylindrical sample. The simulated sample allows for absolute sensitivity comparisons amongst the resonator designs. Experimentally, a minuscule amount of lithium phthalocyanine (LiPC) (51) is embedded in Crytoseal (or similar) wax and is used as a point sample. The LiPC sample produces a very sharp line width (less than 0.05 mT) in the presence of oxygen (narrower without oxygen present), saturates at large values of $\mathbf{B}_{1r}$, and one needs very little sample volume to observe the signal. Therefore the use of LiPC allows for a fair comparison between all resonators by using the same sample throughout the experiments. The term "minuscule" is defined as enough sample to observe a signal in the Bruker MD5W1 without causing line broadening in the micro-helix geometry. Such line broadening is due to a radiation dampening-like behavior caused by the very-large filling factor η.

Two EPR signal parameters were calculated in order to compare different resonant structures: i) unsaturable signal represents the EPR intensity at a given incident power, while ii) saturable signal represents the EPR intensity at a given microwave magnetic field that approaches the limit of saturation, i.e. the maximum achievable signal ($\mathrm{P}_{1/2}$). For pulse experiments, the saturable signal is proportional to the EPR echo intensity in a two-pulse electron spin-echo (ESE) experiment. A 0.4 mm outer diameter and 0.3 mm inner diameter quartz capillary (QSIL GmbH, Ilmenau, Germany) with a 0.2 mm^3 ice sample ($\epsilon_r = 3.17 - i0.0035$, Ref. 52) was used in the simulations. The signal-to-noise ratio for measured data is calculated by the ratio of the acquired signal mean to the standard deviation of the noise voltage, defined by

$$\mathrm{SNR} = \frac{S_p}{2\sigma_{noise}} \tag{S1}$$

where $S_p/2$ is the mean value of the peak-to-peak (or peak for absorption spectra) signal, and σ_{noise} is the standard deviation of the noise. (53) The standard deviation of the noise is calculated using 200 points in an off-resonance region.

Good agreement is shown in Table S1 and in Table 1 in the main text. The lower measured Q-value of the self-resonant micro-helix is due to losses associated with the Polytetrafluoroethylene (PTFE) substrate of the printed-circuit board and losses in the super-glue adhesive. Further work to minimize these losses is underway.

Table S1. Resonator characteristics calculated and measured. Calculations use a 0.1 mm diameter by 0.1 mm height cylindrical sample while measurements use a minuscule amount of lithium phthalocyanine (LiPC) in a 0.4 mm outer diameter and 0.3 mm inner diameter capillary tube. The $P_{1/2}$-values are measured from the power saturation curve and are related to the calculated Λ_{ave}^2. The Λ_{ave} measurements were made by a 2% w/w BDPA (α,γ-Bisdiphenylene-β-phenylallyl; Sigma-Aldrich Chemical; CAS number 35585-94-5) in polystyrene with dimensions of $0.55 \times 0.18 \times 0.08$ mm^3.

Geometry	Freq. [GHz]		Q_0-value		Λ Calc. [mT/W$^{1/2}$]	Λ_{ave} [mT/W$^{1/2}$]		$P_{1/2}$ Meas. [mW]
	Calc.	Meas.	Calc.	Meas.		Calc.	Meas.	
DR (MD5W1)	9.67	9.69	8860	6650	0.60	0.60	–	19.2
LGR (MS3)	9.67	9.69	870	600	0.68	0.68	–	18.4
PMR 6010LM	9.87	9.58	90	61	1.9	1.5	–	17.3
PMR Sapphire	9.87	9.58	190	181	2.9	2.6	2.2	1.8
Micro-Helix	9.78	9.73	360	220	4.1	4.0	3.2	0.8

Power saturation and Λ_{ave} measurements. Power saturation experiments were performed using the LiPC sample. From the power saturation data, an unsaturable signal, saturable signal, and $P_{1/2}$-value measurement can be ascertained. The unsaturable signal is measured at constant microwave power (0.01 mW), while the saturable signal is measured at the power where the EPR signal amplitude is maximum ($P_{1/2}$-value; indicated by $\lozenge$). At the $P_{1/2}$-value, the B_{1r} over the sample is identical in each of the resonators. For the power saturation experiments used in this work the microwave power was stepped in 3 dB increments from 200 mW to 0.2 μW (0-60 dB). Each scan was 30 s over 1 mT with 4096 pts, receiver gain of 60 dB and 100 kHz field modulation at 0.1 mT in all resonators. The over-modulation of the LiPC sample was used to increase the sensitivity in the Bruker commercial resonators while increasing the intrinsic line width (line-height–line-width compromise, discussed in Ref. 54).
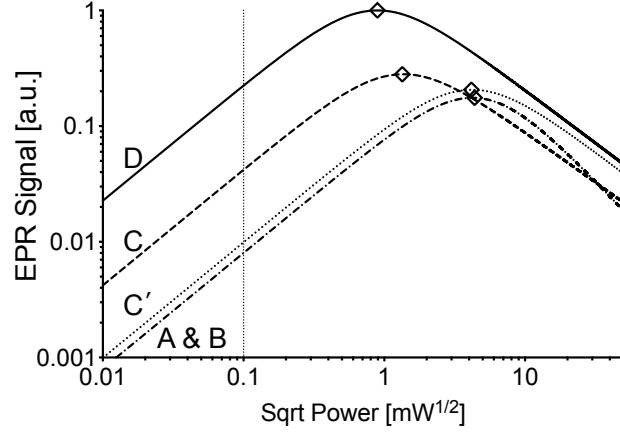
Fig. S3. Power saturation curve of LiPC using various resonators. Power saturation data of LiPC showing the A) Bruker MD5 (dash-dot), and B) Bruker MS3, Ω-type PMR with 0.5 mm sample loop with C) sapphire substrate (dashed) and C′) Rogers 6010LM substrate (dotted), and D) micro-helix (solid). EPR saturable signal is taken at peak signal ($P_{1/2}$-value, constant microwave field; indicated by ◊), while EPR unsaturable signal is taken at 0.01mW(constant microwave power; dotted line).

Shown in Fig. S3 are the measured power saturation data for the series of resonators. The ratio of two $P_{1/2}$-values can be compared to the square of the ratio of Λ_{ave}. The data for the Bruker MS3 and MD5W1, in our hands, lay on top of each other for the LiPC point sample. Simulated and measured EPR signal amplitude characteristics are tabulated in Table S1 and in Table 1 in the main text.

In order to measure the B_{1r} directly, a series of pulse nutation experiments were performed. (7) The pulse nutation experiments were performed with an echo detected EPR signal using a 40 ns $\pi/2$ pulse and a pulse separation of 300 ns. A HA6047 300 W amplifier (HBH Microwave GmbH, Stutensee, DE) was used for all resonators and the power attenuation was adjusted for maximum echo. From the nutation experiment oscillations one can use the equation

$$B_{1r} = \frac{2\pi}{t\gamma} \qquad [\text{G}] \tag{S2}$$

where γ is the gyromagnetic ratio of a free electron and t is the time in seconds for a whole (2π) oscillation, to calculate the B_{1r} in Gauss. The value of B_{1r}, is converted to mT (divide by 10) and normalized to the incident power by

$$\Lambda_{ave} = \frac{B_{1r}}{(P/2^{\varsigma/3})^{1/2}} \qquad [\text{mT/W}^{1/2}] \tag{S3}$$

where P is the maximum power available (in this case, 300 W) and ζ is the attenuation of that power set on the console in dB.

The sample was a 2% w/w BDPA (α,γ-Bisdiphenylene-β-phenylallyl; Sigma-Aldrich Chemical; CAS number 35585-94-5) in polystyrene and, in our laboratory, is used as a pulse EPR standard. The PS and BDPA are fully dissolved in toluene, laid out onto a covered Pyrex Petri dish, and left to evaporate for several days. The sample is then cut and placed in the sample tube for further testing. For a direct measurement of Λ_{ave}, an EPR nutation experiment was performed at three pulse powers using the 2% w/w BDPA in polystyrene and cut to $0.55 \times 0.18 \times 0.08$ mm^3. The micro-helix has measured power conversion efficiency parameter of 3.2 mT/W$^{1/2}$ which corresponds, for an S=1/2 spin system with g=2, to a $\pi/2$ pulse of 20 ns with an incident power of approximately 20 mW. No signal was measurable in the PMR RO6010LM, MS3, and MD5W1 due to lack of sensitivity. However, the PMR with a sapphire substrate has a good efficiency parameter of 2.2 mT/W$^{1/2}$ which corresponds, for an S=1/2 spin system with g=2, to a $\pi/2$ pulse of 20 ns with an incident power of approximately 40 mW. These data are tabulated in Table S1.
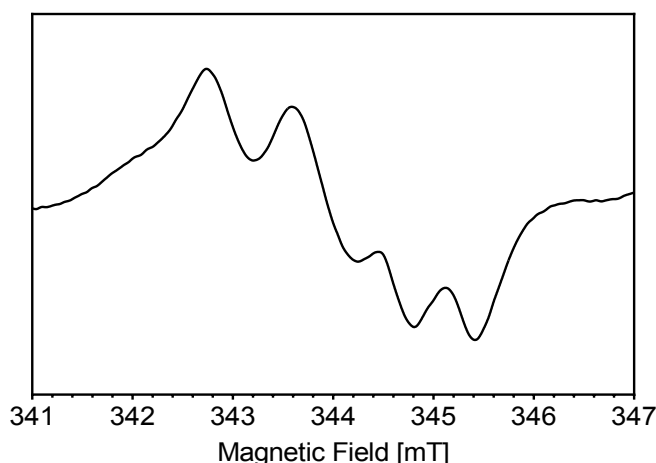
Fig. S4. Continuous-wave EPR of frozen solution photosystem II BBY particles performed in the Bruker MD5W1 dielectric resonator at a temperature of 80 K. A signal-to-noise ratio of approximately 300 is calculated for 636 nL of sample.

Sensitivity comparison of the X-band microhelix to a commercial dielectric resonator. A comparison between the MD5W1 dielectric resonator and the self-resonant micro-helix was performed with the frozen solution of photosystem II BBY particles at a temperature of 80 K. A continuous-wave EPR experiment was performed to compare the EPR signal obtained with 85 nL volume in the micro-helix, shown in Fig. 3A in the main text. The spectrum was collected by sweeping 10 mT in 1 minute (4096 points) with a modulation rate of 100 kHz and an amplitude of 0.5 mT. The data are averaged 49 times for a total time of 49 minutes at an incident power of 3.1 μW, shown in Fig S4A. This power was chosen to compare the two samples at approximately the same microwave magnetic field incident

on the sample. The photosystem II sample was placed in a 0.3 mm inner diameter quartz tube with a sample height of 9 mm (636 nL) and centered in the dielectric cavity. A signal-to-noise ratio of approximately 300 is calculated for the 636 nL of sample. Normalizing the signal-to-noise ratio with the volume yields a factor of approximately 5 improvement of absolute spin sensitivity using the self-resonant micro-helix compared to the MD5W1.

Qualitative sensitivity comparison of the X-band microhelix to high-frequency single-mode resonators. Simulations were performed in commercial finite-element modeling software, Ansys Electronics Desktop with HFSS (High Frequency Structure Simulator; v. 19.1), comparing a cylindrical TE_{011} cavity at W-band to the micro-helix geometry using a 85 nL frozen solution sample. Typically, due to the Boltzmann factor, an increase of the operating frequency leads to a proportional increase of the probability of the energy excited during resonance. The EPR signal increase from the Boltzmann factor is accounted for in the magnetic susceptibility χ in Eq. 1 of the main text. However, the ηQ product (resonator efficiency; Λ_{ave}) and g-strain contribute to the overall sensitivity. Nevertheless, assuming no g-anisotropy, the W-band TE_{011} exhibits only a factor of approximately 3 in improved EPR signal intensity compared to the micro-helix geometry at X-band.

As the frequency becomes even higher, the resonator efficiency decreases due to losses on the surface of the resonator. For example, the Bruker 263 GHz single-mode resonator has a reported Λ_{ave}-value of 0.7 mT/W$^{1/2}$. (55) Although the frequency is approximately 27 fold higher compared to X-band, the Λ_{ave} is approximately half of the cylindrical TE_{011} cavity at W-band. The lower Λ_{ave} leads to only a factor of five in EPR signal improvement compared to the micro-helix at X-band. However, the effects of line broadening through g-strain become more severe as the operating frequency increases leading to a reduced signal-to-noise ratio.

Therefore, the micro-helix geometry opens up the possibility to perform multi-frequency EPR on the same sample from X-band to 263 GHz. Using a 0.4 mm outer diameter capillary, a sample can be placed in the micro-helix at X-band and the same sample can then be inserted into a W-band (94 GHz) or 263 GHz cavity. This ability allows for complimentary techniques to be used for disentangling the angle dependencies of hyperfine-tensor interactions.

Crystal rotation and simulation. In the current setup, the entire probe head is rotated within the magnet. Since the setup is axially symmetric, this allows for full rotation in one crystal plane over 180 degrees. From this, the Laboratory Frame is fixed in the EasySpin simulations and the rotation around the L_3-axis is performed, assuming the static magnetic field is in the L_1-axis, per Fig. 4B in the main text. Since the micro-helix assembly uses an SMA connector, it is straightforward to modify the angle by using a 90° bend. This would align B_1 along the L_2-axis, where a partial rotation would be feasible. Finally, if necessary, a third rotation would be feasible by rotating the sample by 90° and performing another partial rotation.

From the crystal structure (PDB ID: 4XDC) the molecular frame of the H-cluster can be determined. Using the distal iron (Fe_d) as the origin, the molecular frame is calculated and tabulated in Table S2. The three axes for the molecular frame were chosen as i) an axis from the distal iron (Fe_d) to

the proximal iron (Fe_p), ii) the normal of a plane calculated from the proximal iron, distal iron, and the nitrogen of the ADT-ligand (Fe_p-Fe_d-N_1), and iii) the cross product of (i) into (ii). Since the [FeFe]-hydrogenase forms an assymetric unit, a second molecular-frame (Molecular-Frame B) is needed to describe the system and is chosen in the same way as for the Molecular-Frame A. The crystal symmetry of P1 2_1 1 is taken into account in the EasySpin simulations and duplicates the molecular frames from Site I to Site II, illustrated in Fig. 5B in the main text. The g-tensor is then plotted with respect to the molecular frame (See EasySpin documentation: http://easyspin.org/documentation/erot.html and http://easyspin.org/documentation/frames.html).

Comparison of the proposed g-tensor by Adamska-Venkatesh *et al.* from Ref. 38 and the g-tensor proposed in this work is shown in Fig. S5. It was previously proposed that the *x*-axis pointed towards the ADTligand and the *z*-axis was along the Fe_d-Fe_p axis with a CN_d-Fe_d-g_z angle of 117°, which coordinates with the chosen molecular frame. According to the g-Tensor solved from the single-crystal EPR data collected in this work, the whole coordinate system deviates from the Fe_d-Fe_p axis by only 10.1°. However, the proposed g-tensor orientation has the *x*-axis pointing outward at the open coordination site and the *z*-axis is within the plane of the CO and CN ligands.
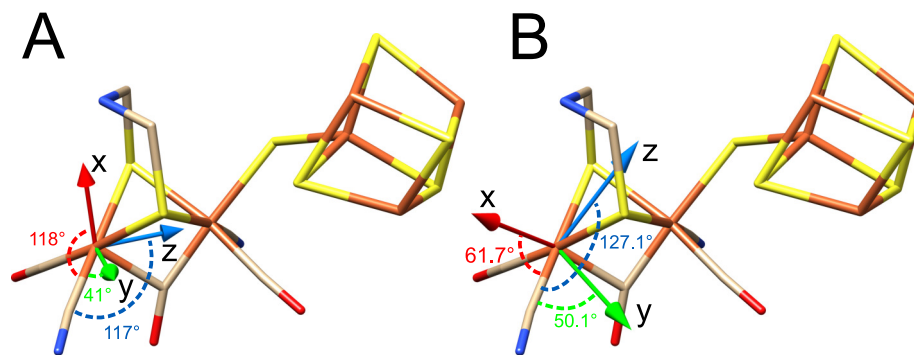
Fig. S5. Comparison of the *g*-tensor proposed by Adamska-Venkatesh *et al.* (*38*) and the current proposed *g*-tensor from this work. A) The proposed g-tensor by Adamska-Venkatesh *et al.* overlaid onto the H-cluster from PCB ID 3C8Y. (Adapted from from Ref. 38 with permission from the PCCP Owner Societies.) B) The proposed g-tensor of this work overlaid onto the H-cluster from PCB ID 4XDC.

The simulation is setup with 9 unknowns: the three axes of the crystal frame that relates how the crystal is orientated in the laboratory frame, the three axes of the g-tensor of the first molecule (g-Tensor A) and how it relates to the Molecular-Frame A, and the three axes of the g-tensor of the second molecule (g-Tensor B) and how it relates to the Molecular-Frame B. However, we can assume that the g-tensor of the second molecule will be almost the same as the first molecule, based on similar research at W-band with photosystem II. (5, 56) From this knowledge, we can limit the deviation of the g-tensor of the second molecule (g-Tensor B) with respect to the first (g-Tensor A). The crystal frame and g-Tensor A were set to vary from a whole rotation, while g-Tensor B was limited to ±10 degree difference at each axis compared to g-Tensor A. The principal g-values were obtained from previous frozen solution EPR experiment in Ref. 16 (g-values: [1.999, 2.039, 2.097] corresponding to x, y, and z, respectively).

A particle swarm optimization algorithm with 10,000 particles was used to find the solution. Each run was allowed to converge in 10 iterations and checked if a local minimum was found. Simulations were re-run until a good fit was established. The MatLab code can be found at: https://act-epr.org/data. The rotational matrices to project to the Laboratory Frame are found in Table S2.

Since only one rotation plane was recorded, the fit of the g-tensor orientation may not be unique. At least one additional plane should be obtained to ensure a unique fit with P1 2_1 1 symmetry. However a very good fit is currently found. Rotation is straightforward since the micro-helix assembly uses an SMA connector. The angle can be modified and the B_1 can be orientated along the L_2-axis (Fig. 5B in the main text) by using a 90° bend. The whole micro-helix insert, as done in this work, or the static magnetic field can be rotated, illustrated in Fig. 5C.

Table S2. Rotational matrices for the crystal frame with respect to the laboratory frame and the g-tensor with respect to the molecular frame. The crystal frame and g-tensor are found by fitting the data in Fig. 4 with the molecular frame from PDB ID 4XDC.

	Crystal Frame		
	a	b	c
L_1	+0.273	−0.162	−0.948
L_2	−0.022	−0.987	+0.162
L_3	−0.962	+0.023	−0.273

	Molecular-Frame A			Molecular-Frame B		
	x	y	z	x	y	z
a	−0.331	−0.938	+0.107	−0.595	−0.666	−0.450
b	−0.770	+0.203	−0.605	+0.456	−0.740	+0.494
c	+0.545	−0.283	−0.789	−0.662	+0.089	+0.744

	g-Tensor A			g-Tensor B		
	x	y	z	x	y	z
a	+0.476	−0.484	+0.735	+0.377	−0.605	−0.701
b	−0.400	+0.625	+0.671	−0.388	+0.584	−0.713
c	+0.783	+0.613	−0.103	+0.841	+0.541	−0.015